Monthly Notices
of the
ROYAL ASTRONOMICAL SOCIETY

Mon. Not. R. Astron. Soc. **409,** 12–21 (2010) doi:10.1111/j.1365-2966.2010.17093.x

Modelling *Herschel* observations of infrared-dark clouds in the Hi-GAL survey⋆

D. Stamatellos,[1]† M. J. Griffin,[1] J. M. Kirk,[1] S. Molinari,[2] B. Sibthorpe,[3] D. Ward-Thompson,[1] A. P. Whitworth[1] and L. A. Wilcock[1]

[1]*School of Physics & Astronomy, Cardiff University, Cardiff CF24 3AA*
[2]*INAF-IFSI, Fosso del Cavaliere 100, 00133 Roma, Italy*
[3]*UK Astronomy Technology Centre, Royal Observatory, Blackford Hill, Edinburgh EH9 3HJ*

Accepted 2010 May 26. Received 2010 May 24; in original form 2010 January 26

ABSTRACT

We demonstrate the use of the 3D Monte Carlo radiative transfer code PHAETHON to model infrared-dark clouds (IRDCs) that are externally illuminated by the interstellar radiation field (ISRF). These clouds are believed to be the earliest observed phase of high-mass star formation, and may be the high-mass equivalent of lower mass pre-stellar cores. We model three different cases as examples of the use of the code, in which we vary the mass, density, radius, morphology and internal velocity field of the IRDC. We show the predicted output of the models at different wavelengths chosen to match the observing wavebands of *Herschel* and *Spitzer*. For the wavebands of the long-wavelength Spectral and Photometric Imaging Receiver (SPIRE) photometer on *Herschel*, we also pass the model output through the SPIRE simulator to generate output images that are as close as possible to the ones that would be seen using SPIRE. We then analyse the images as if they were real observations, and compare the results of this analysis with the results of the radiative transfer models. We find that detailed radiative transfer modelling is necessary to accurately determine the physical parameters of IRDCs (e.g. dust temperature, density profile). This method is applied to study G29.55+00.18, an IRDC observed by the *Herschel* Infrared Galactic Plane Survey (Hi-GAL), and in the future it will be used to model a larger sample of IRDCs from the same survey.

Key words: radiative transfer – methods: numerical – stars: formation – ISM: clouds – dust, extinction – ISM: structure.

1 INTRODUCTION

High-mass stars evolve somewhat differently from low-mass stars. There appear to be (at least) four main evolutionary stages of high-mass star formation (e.g. Zinnecker & Yorke 2007): infrared-dark clouds (IRDCs), hot molecular cores, compact H II regions (including hypercompact and ultracompact H II regions) and classical H II regions.

The earliest observed phase of high-mass star formation is the IRDC stage. IRDCs are very dense, massive interstellar clouds in which high-mass stars are believed to form. They were first identified in infrared (IR) surveys, by the *Infrared Space Observatory* (*ISO*; Perault et al. 1996) and the *Midcourse Space Experiment* (*MSX*; Egan et al. 1998), as denser, higher mass and more distant analogues to pre-stellar cores (Ward-Thompson et al. 1994, 2007), from which lower mass stars form (e.g. solar-type stars). In fact, IRDCs are so dense that they are optically thick even at IR wavelengths (∼8–24 μm). In many of these clouds there is little or no detectable star formation (e.g. Parsons, Thompson & Chrysostomou 2009).

The mass of an IRDC can be hundreds, or even thousands of solar masses (e.g. Rathborne et al. 2009). Often, dense, dark cores can be seen within each cloud. These are known as infrared-dark cores, and can have masses of up to ∼100 $M_{\odot}$, and are typically only 0.1 pc or less in radius. Hence they have densities of up to $\sim 10^{12}$ hydrogen molecules m^{-3} (e.g. Carey et al. 1998, 2000; Egan et al. 1998). These are the most likely candidate sites of high-mass star formation.

The *Herschel Space Observatory* was launched on 2009 May 14, and carries a 3.5-m diameter telescope and three scientific instruments designed to carry out imaging and spectroscopy (Pilbratt et al. 2008, 2010). The Spectral and Photometric Imaging Receiver

⋆*Herschel* is an ESA space observatory with science instruments provided by European-led Principal Investigator consortia and with important participation from NASA.

†E-mail: d.stamatellos@astro.cf.ac.uk

(SPIRE[1]) is the long-wavelength camera on board *Herschel* (Griffin et al. 2009, 2010). The *Herschel* Infrared Galactic Plane Survey (Hi-GAL) is a *Herschel* Open Time key project that is mapping the inner Galaxy in five bands between 60 and 500 μm (Molinari et al. 2010a,b). Hi-GAL will map the area common to the *Spitzer* GLIMPSE and MIPSGAL (Rieke et al. 2004) and *MSX* (Price et al. 2001) Galactic plane surveys, but at far-infrared (FIR) and submillimetre wavelengths. Hence, the IRDCs will be seen in emission, in contrast with the previous surveys. One of the science goals of Hi-GAL is to determine the physical properties of IRDCs and hence constrain the initial conditions of high-mass star formation.

In this paper we demonstrate the use of the 3D Monte Carlo radiative transfer code PHAETHON in converting 2D imaging data of IRDCs from the Hi-GAL survey into the physical parameters of the clouds being studied, with particular emphasis on the data from SPIRE. In Section 2 we describe the radiative transfer code and the specific input parameters used in this paper. In Section 3 we present radiative transfer models of three IRDCS with different morphologies (spherical, flattened and turbulent). In Section 4 we use the SPIRE photometer simulator to produce simulated observations of the IRDC models, and in Section 5 we compare the radiative transfer models with the simulated observations. In Section 6, we apply this method to determine the properties of G29.55+00.18, an IRDC from the Hi-GAL survey. Finally, in Section 7 we summarize our results.

2 NUMERICAL METHOD: MONTE CARLO RADIATIVE TRANSFER

2.1 Code overview

The radiative transfer calculations are performed using PHAETHON,[2] a 3D Monte Carlo radiative transfer code (Stamatellos 2003; Stamatellos & Whitworth 2003, 2005; Stamatellos et al. 2004, 2005; Stamatellos, Whitworth & Ward-Thompson 2007). The code uses a large number of monochromatic luminosity packets to represent the radiation sources in the system (stars and/or the ambient radiation field). The luminosity packets are injected into the system and interact (are absorbed, re-emitted, scattered) stochastically with it. If a luminosity packet is absorbed its energy is added to the local region and raises the local temperature. To ensure radiative equilibrium this packet is re-emitted immediately with a new frequency chosen from the difference between the local cell emissivity before and after the absorption of the packet (Bjorkman & Wood 2001; Baes et al. 2005).

The input parameters of the code are (i) the density profile of the system, (ii) the dust properties (e.g. opacity) and (iii) the radiation sources present (e.g. ambient radiation field and/or stars). The code calculates the dust temperature and produces observables: (i) the spectral energy distribution (SED) of the system at different viewing angles and (ii) synthetic images of the system at different viewing angles and at different wavelengths.

[1] SPIRE has been developed by a consortium of institutes led by Cardiff University (UK) and including University of Lethbridge (Canada); NAOC (China); CEA, LAM (France); IFSI, University of Padua (Italy); IAC (Spain); Stockholm Observatory (Sweden); Imperial College London, RAL, UCL-MSSL, UKATC, University of Sussex (UK) and Caltech, JPL, NHSC, University of Colorado (USA). This development has been supported by national funding agencies: CSA (Canada); NAOC (China); CEA, CNES, CNRS (France); ASI (Italy); MCINN (Spain); SNSB (Sweden); STFC (UK) and NASA (USA).

[2] http://www.astro.cf.ac.uk/pub/Dimitrios.Stamatellos/phaethon

Table 1. IRDC parameters used in the radiative transfer models. n_c: cloud central density; r_0: cloud flattening radius; R_{cloud}: cloud extent; M_{cloud}: cloud mass; d_{cloud}: cloud distance.

	Spherical	Flattened	Turbulent
n_c (cm^{-3})	5×10^6	10^7	5×10^6
r_0 (pc)	0.08	0.04	0.08
R_{cloud} (pc)	1	1	1.5
M_{cloud} ($M_\odot$)	1300	510	27 200
d_{cloud} (kpc)	2	2	2

2.2 External radiation field and dust properties

A starless IRDC is assumed, hence the cloud is only heated by the ambient radiation field. For the ambient radiation field we adopt a revised version of the Black (1994) interstellar radiation field (ISRF). This consists of radiation from giant stars and dwarfs, thermal emission from dust grains, cosmic background radiation and mid-IR emission from transiently heated small polycyclic aromatic hydrocarbon (PAH) grains (André et al. 2003). This radiation field represents well the ISRF in the solar neighbourhood, but it is probably an underestimate of the ambient radiation field in the Galactic plane. An enhanced ambient radiation field could result in higher dust temperatures at the surface of the clouds, but the temperatures in the central cloud regions are not expected to be significantly higher (only a few degrees). The luminosity packets representing the ambient radiation field (typically a few $\times 10^{10}$ packets) are injected from the outside of the cloud with injection points and injection directions chosen to mimic an isotropic radiation field incident on the cloud (Stamatellos et al. 2004, 2007).

The dust grains in dense clouds are expected to coagulate and accrete ice mantles, thus we use the Ossenkopf & Henning (1994) opacities for the standard Mathis, Rumpl & Nordsieck (1977) interstellar grain mixture (53 per cent silicate and 47 per cent graphite), with grains that have coagulated and accreted thin ice mantles over a period of 10^5 yr at densities 10^6 cm^{-3}. We assume a gas-to-dust mass ratio of 100.

3 RADIATIVE TRANSFER MODELS OF IRDCs

We model three different cloud geometries: (i) a spherical cloud, (ii) a flattened cloud and (iii) a turbulent cloud with substructure. We also vary the mass, density and radius. The parameter values are chosen so as to illustrate some of the variety of parameter values that the code can handle. The parameters of each of the three cases are listed in Table 1.

3.1 Spherical IRDC

For the spherical cloud we adopt a Plummer-like density profile (Plummer 1915),

$$n(r) = n_c \frac{1}{\left[1 + (r/r_0)^2\right]^2}, \quad (1)$$

where n_c is the density at the centre of the cloud, and r_0 is the extent of the region in which the density is approximately uniform. This density profile is consistent with observations of low-mass

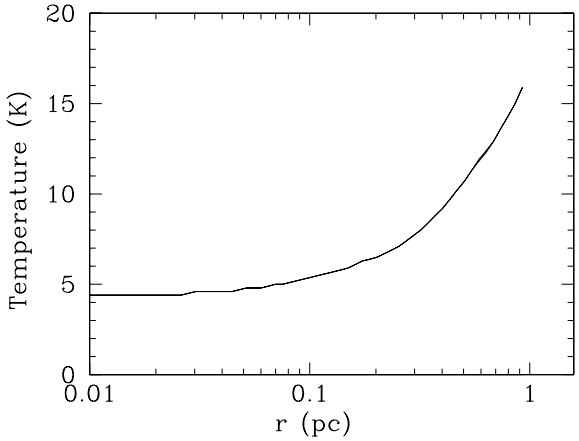

Figure 1. Dust temperature profile of a spherical IRDC.

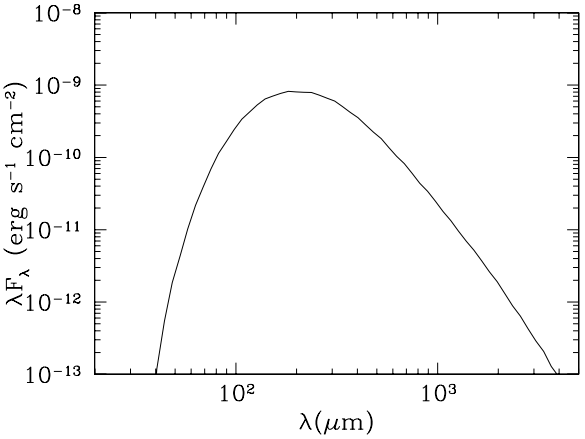

Figure 2. SED of a spherical cloud at a distance of 2 kpc.

cores in nearby star-forming clouds, such as L1544, L63 and L43 (e.g. Kirk, Ward-Thompson & André 2005; Kirk, Ward-Thompson & Crutcher 2006; Kirk, Ward-Thompson & André 2007), and has been used to model such clouds (Whitworth & Ward-Thompson 2001). The values of these parameters are given in Table 1. The mass of the cloud is 1300 $M_\odot$.

Fig. 1 shows that the temperature in the cloud drops from ∼16 K at the edge of the cloud to ∼4 K at the centre of the cloud. The central dust temperature is 2–3 K lower than the typical temperatures in the central regions of low-mass (i.e. a few solar masses) clouds (∼7 K; e.g. Stamatellos & Whitworth 2003; Stamatellos et al. 2004). This is due to the much higher mass and extinction of the IRDC. Heating from cosmic rays, which is not included in our models, may increase the temperature in the centre of the cloud to ∼5 K. Additionally, a stronger external radiation field in the Galactic plane could also possibly increase the temperature by a few degrees.

Fig. 2 shows that the SED of the cloud peaks at around 200 μm, consistent with the low temperatures in the cloud. Because the temperature gradient in the IRDC is larger than the temperature gradient in a low-mass core, the SED is broader.

3.2 Flattened IRDC

For the flattened cloud we use a density profile of the form

$$n(r,\theta) = n_{\rm c}\,\frac{1 + A\,(r/r_0)^2\sin^p(\theta)}{\left[1+(r/r_0)^2\right]^2}\,, \qquad (2)$$

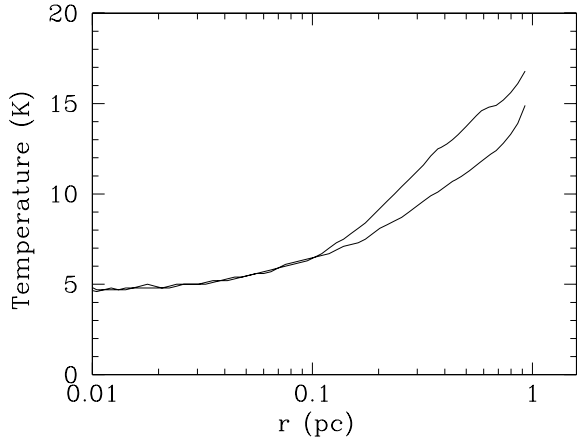

Figure 3. Dust temperature profile of a flattened cloud at two different directions in the cloud. The bottom line corresponds to the mid-plane of the flattened structure, whereas the upper line corresponds to the direction perpendicular to the mid-plane.

where $n_{\rm c}$ is the density at the centre of the cloud, and r_0 is the extent of the region in which the density is approximately uniform (see Stamatellos et al. 2004). The values of these parameters are given in Table 1. The parameter A determines the equatorial-to-polar optical depth ratio e, i.e. the maximum optical depth from the centre to the surface of the cloud (which occurs at $\theta = 90^\circ$), divided by the minimum optical depth from the centre to the surface of the cloud (which occurs at $\theta = 0^\circ$ and 180°). The parameter p determines how rapidly the optical depth from the centre to the surface rises with increasing θ, i.e. going from the north pole at $\theta = 0^\circ$ to the equator at $\theta = 90^\circ$. In this model we assume $e = 1.03$, i.e. a slightly flattened cloud, and $p = 4$. This geometry may be more realistic than the spherical cloud presented in the previous section. The mass of the cloud is 510 $M_\odot$ (see Table 1).

Fig. 3 shows that the temperature profile in the cloud is similar to the case of the spherical cloud; the temperature drops from 18 K at the edge to 5 K in the centre of the cloud. However, due to the flattened cloud geometry the cloud 'equator' is colder than the cloud 'poles'.

Fig. 4 shows that the SED of the cloud is also similar to that of the spherical cloud. There is no dependence on the viewing angle despite the fact that the optical depth to the centre of the cloud becomes $\tau_{\rm cloud} \sim 1$ at ∼200 μm. This is because the temperature

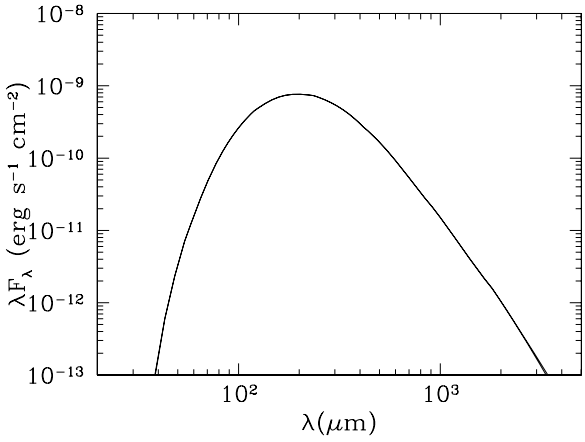

Figure 4. SED of a flattened cloud at a distance of 2 kpc.

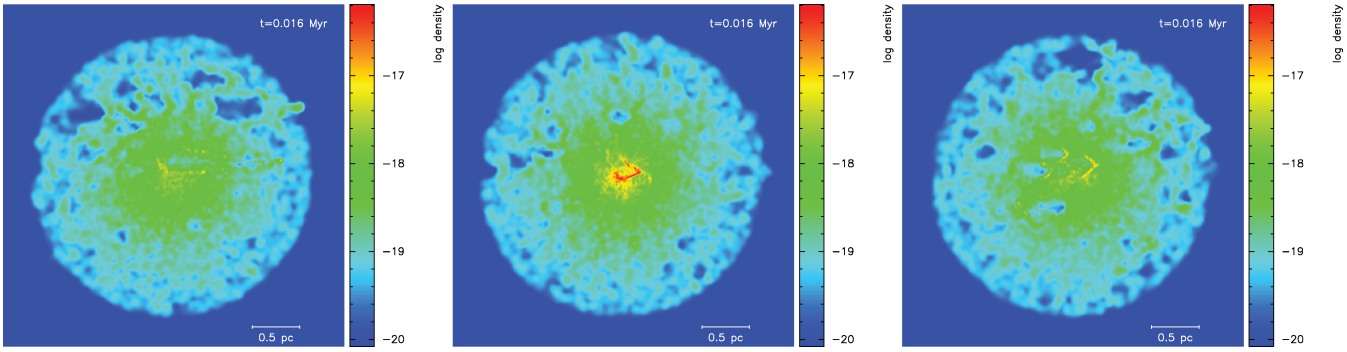

Figure 5. Density on the $y = -0.2$ pc (left-hand panel), $y = 0$ pc (centre) and $y = +0.2$ pc (right-hand panel) planes for a turbulent IRDC. The density is given in units of g cm^{-3}.

varies with the direction in the cloud only in the outer region of the cloud, which is optically thin even at wavelengths up to ∼200 μm.

3.3 Turbulent IRDC

We finally examine a more realistic cloud geometry, i.e. a turbulent cloud. To produce this cloud we start off with a spherical cloud having a density profile

$$n(r) = n_{\rm c} \frac{1}{1 + (r/r_0)^2}\,, \qquad (3)$$

where $n_{\rm c}$ is the density at the centre of the cloud and r_0 is the extent of the region in which the density is approximately uniform. Note that this profile is less steep than the profile used for the spherical IRDC, hence the higher mass of this cloud.

The values of the parameters are again given in Table 1. The mass of the cloud is 27 200 $M_\odot$. A large turbulent velocity field ($\alpha = 0.5$) is imposed on the cloud (e.g. Goodwin, Whitworth & Ward-Thompson 2004), and the cloud is evolved using the smoothed particle hydrodynamics (SPH) code DRAGON for enough time to produce substructure, i.e. until cores form in the cloud (e.g. Stamatellos et al. 2007). DRAGON is a gravitational hydrodynamics code which invokes a large number of particles to represent a physical system. It uses an octal tree (to compute gravity and find neighbours), adaptive smoothing lengths, multiple particle time-steps, and a second-order Runge–Kutta integration scheme. The resulting cloud is shown in Fig. 5, in which we plot its density on three planes ($y = -0.2$ pc, left-hand panel; $y = 0$ pc, centre and $y = +0.2$ pc, right-hand panel).

We perform a radiative transfer simulation for this cloud using the method of Stamatellos & Whitworth (2005). The calculated dust temperature is presented in Fig. 6. The dust temperature is similar to the temperature calculated in the previous cases. However, the temperature distribution at a particular distance from the centre of the cloud is broader due to the clumpiness of the cloud. Fig. 7 shows that the SED of the cloud peaks at longer wavelengths than in the previous two cases, as the cloud is more massive and consequently it is cooler.

4 SPIRE-SIMULATED OBSERVATIONS

Simulated observations of the modelled IRDCs are performed to assess the impact of instrument systematics. The simulations are produced using V2.31b of the SPIRE photometer simulator (Sibthorpe, Chanial & Griffin 2009). This software simulates both the SPIRE instrument and the *Herschel* observing modes. The simulations are performed in a configuration which matches the Hi-GAL observations.

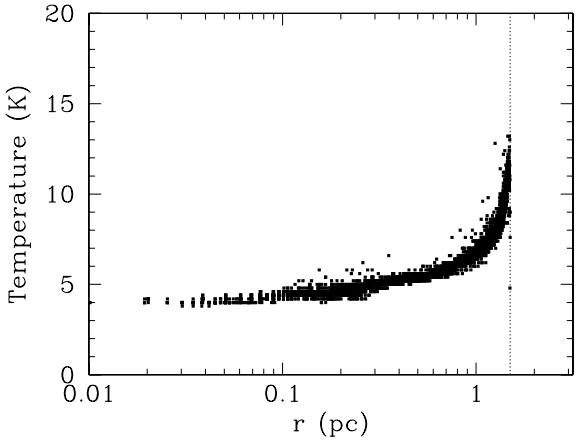

Figure 6. Dust temperature of a turbulent IRDC. The points correspond to different locations in the cloud.

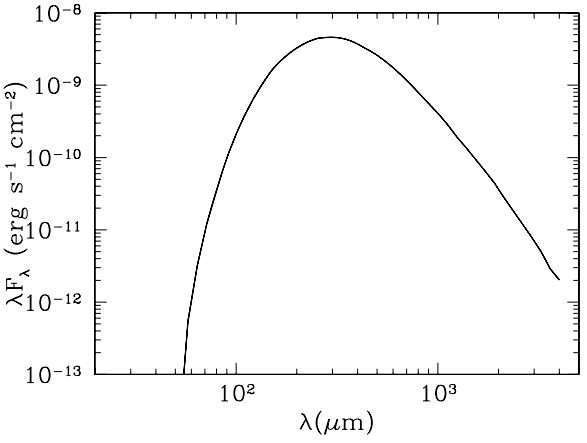

Figure 7. SED of a turbulent IRDC at a distance of 2 kpc.

The fast scanning speed (60 arcsec s^{-1}) option is used (see the SPIRE Observers' Manual[3]), and the observations are made in the SPIRE parallel mode, to match the Hi-GAL mapping mode. These observations are performed by continuously scanning the telescope backwards and forwards in a raster pattern while the instruments continuously take data.

[3] http://herschel.esac.esa.int/Documentation.shtml

For Hi-GAL two maps are obtained by scanning first along one axis of the instrument array, and then scanning along the perpendicular axis of the array. This provides redundancy in the data, allowing for the use of maximum likelihood techniques to be used in the subsequent data reduction (Sibthorpe et al. 2009).

Realistic noise with a $1/f$ spectrum is simulated with each of the SPIRE bolometers using independent noise parameters based on pre-flight test data. Thermal drifts are not included in these simulations as the information is not available to model these accurately. However, the *Herschel*/SPIRE pipeline will automatically remove these drifts, making their omission from these simulations insignificant.

The simulated data are calibrated and reduced from time-line data to maps using a simple map-maker. Maps at the three SPIRE bands, 250, 350 and 500 μm are obtained, having full width half-maximum (FWHM) beams sizes of 18, 25 and 36 arcsec, respectively.

5 COMPARISON OF IRDC MODELS TO THE SIMULATED OBSERVATIONS

5.1 Maps

Synthetic maps of the plane-of-sky intensity distribution of the three IRDCs are produced using the radiative transfer model. The maps are produced at eight wavebands (8, 15, 70, 160, 250, 350, 500 and 500 μm) that replicate the filter sets of recent telescope facilities. The 8- and 15-μm wavelengths match two bands from the *MSX* satellite (Price et al. 2001). The near-IR 8 μm is also found on *Spitzer*'s IRAC camera (Fazio et al. 2004). The 8-μm filter can show strong emission from PAH grains (Flagey et al. 2006). The radiative transfer model does not include transiently heated small grains. These grains dominate the emission at some IR bands (e.g. Li & Draine 2001). In this paper we focus at longer wavebands ($\lambda > 70$ μm), where there is no emission from such grains.

The FIR bands at 70- and 160-μm bands match approximately the 70- and 160-μm bands of *Spitzer*'s MIPS camera (Rieke et al. 2004), the N60 and N160 bands of *Akari* (Kawada et al. 2007) and the 70 and 160 bands of *Herschel*'s PACS[4] camera (Poglitsch & Altieri 2009; Poglitsch et al. 2010). The submillimetre bands at 250, 350 and 500 μm match approximately the filter set of *Herschel*'s SPIRE (Griffin et al. 2009; Griffin, in preparation) camera and the BLAST balloon experiment (Pascale et al. 2008). The 850-μm band matches approximately the long-wavelength filter of the Submillimetre Common-User Bolometer Array (SCUBA; Holland et al. 1999,) and SCUBA2 (Holland et al. 2006) on the James Clerk Maxwell Telescope (JCMT). The 500-μm band is also roughly equivalent to SCUBA's and SCUBA2's 450-μm band (Holland et al. 1999, 2006).

Given a synthetic map of intensity it is possible to simulate the observing process and produce simulated observations that match the resolution and expected instrumental characteristic of the chosen camera. As described in Section 4, we have used the SPIRE simulator to produce simulated observations for the 250–500 μm data.

[4] PACS has been developed by a consortium of institutes led by MPE (Germany) and including UVIE (Austria); KU Leuven, CSL, IMEC (Belgium); CEA, LAM (France); MPIA (Germany); INAF-IFSI/OAA/OAP/OAT, LENS, SISSA (Italy) and IAC (Spain). This development has been supported by the funding agencies BMVIT (Austria), ESA-PRODEX (Belgium), CEA/CNES (France), DLR (Germany), ASI/INAF (Italy) and CICYT/MCYT (Spain).

Fig. 8 shows the model IRDCs before (blue colour table) and after (red colour table) they have been processed into simulated observations. The columns are labelled at the top with the wavelength; the rows are labelled on the right-hand side with the description of the cloud. The maps show a radius of 1.1 pc around the centre of each cloud. The pixel size of the model cloud maps at all wavelengths is 0.019 pc (1.9 arcsec) for the spherical and flattened cloud and 0.028 (2.9 arcsec) for the turbulent cloud. The pixel sizes of the 250-, 350- and 500-μm maps are approximately a third of the SPIRE beam FWHMs, corresponding to 0.058 pc (6 arcsec), 0.097 pc (10 arcsec) and 0.116 pc (12 arcsec) at 250, 350 and 500 μm, respectively. The 8- and 15-μm bands are not shown in Fig. 8, as they simply show up as dark clouds against a bright background.

IRDCs have been identified in large numbers from IR surveys (Simon et al. 2006; Peretto & Fuller 2009) as higher mass and more distant analogues to the optically dark clouds of gas and dust seen in silhouette against a bright background in V-band surveys (e.g. Barnard, Frost & Calvert 1927; Lynds 1962). Starting at the shortest wavelength in Fig. 8 (70 μm) this extinction can be seen in the spherical and flattened model clouds as a central dark patch. The size of this patch decreases with increasing wavelength until 500 μm where it has either closed up entirely or can no longer be resolved. We note that the size of the emitting region at 500 μm is approximately the same size as the dark region at 70 μm.

The substructure of the turbulent cloud which is evident in the model images is hardly visible in the simulated images due to the angular resolution of the simulations being larger than the length-scale of the substructure at the assumed distance of the IRDC (2 kpc).

Table 2 lists the FWHM of 2D Gaussians fitted to each of the 250–500 μm model clouds. These show quantitatively that the FWHM of the emitting region also decreases with increasing wavelength. This can be ascribed to the centre-to-edge temperature gradient. Cold dust located towards the centre of the cloud will preferentially radiate at longer wavelengths, whereas warmer dust located towards the edge of the cloud will preferentially radiate at shorter wavelengths. The wavelength-dependent size of the cloud is also visible in the simulated observations. However, the central extinction hole is only resolved for the spherical cloud at 250 μm.

5.2 Radial profiles

Fig. 9 shows radial profiles of each of the IRDCs shown in Fig. 8. Each column shows a single model cloud as annotated in the upper plot (spherical, flattened or turbulent), while each row of panels represents a particular property or set of parameters. No a priori knowledge (e.g. about the density profile and the dust temperature) is assumed whilst generating the radial profiles.

We compute an equivalent semimajor axis a_i for each pixel i with coordinates (x_i, y_i) by assuming that it lies on an ellipse with the same origin, position angle and axis ratio r_{350} as the equivalent 350-μm cloud (i.e. the simulated observations use the axis ratio of the 350-μm simulated cloud). The spherical and turbulent models have axial ratios of ∼1.0 and the flattened model cloud has an axial ratio of ∼1.5; it is assumed that the clouds' axes have a position angle of zero. The equivalent semimajor axis a_i is given by

$$a_i^2 = (x_{\rm cen} - x_i)^2 + [r_{350}(y_{\rm cen} - y_i)]^2, \quad (4)$$

where $(x_{\rm cen}, y_{\rm cen})$ are the coordinates of the centre of the cloud. Once a_i is known, we bin the pixels into bins of width Δa and compute the mean and standard deviation of the intensities of the pixels in

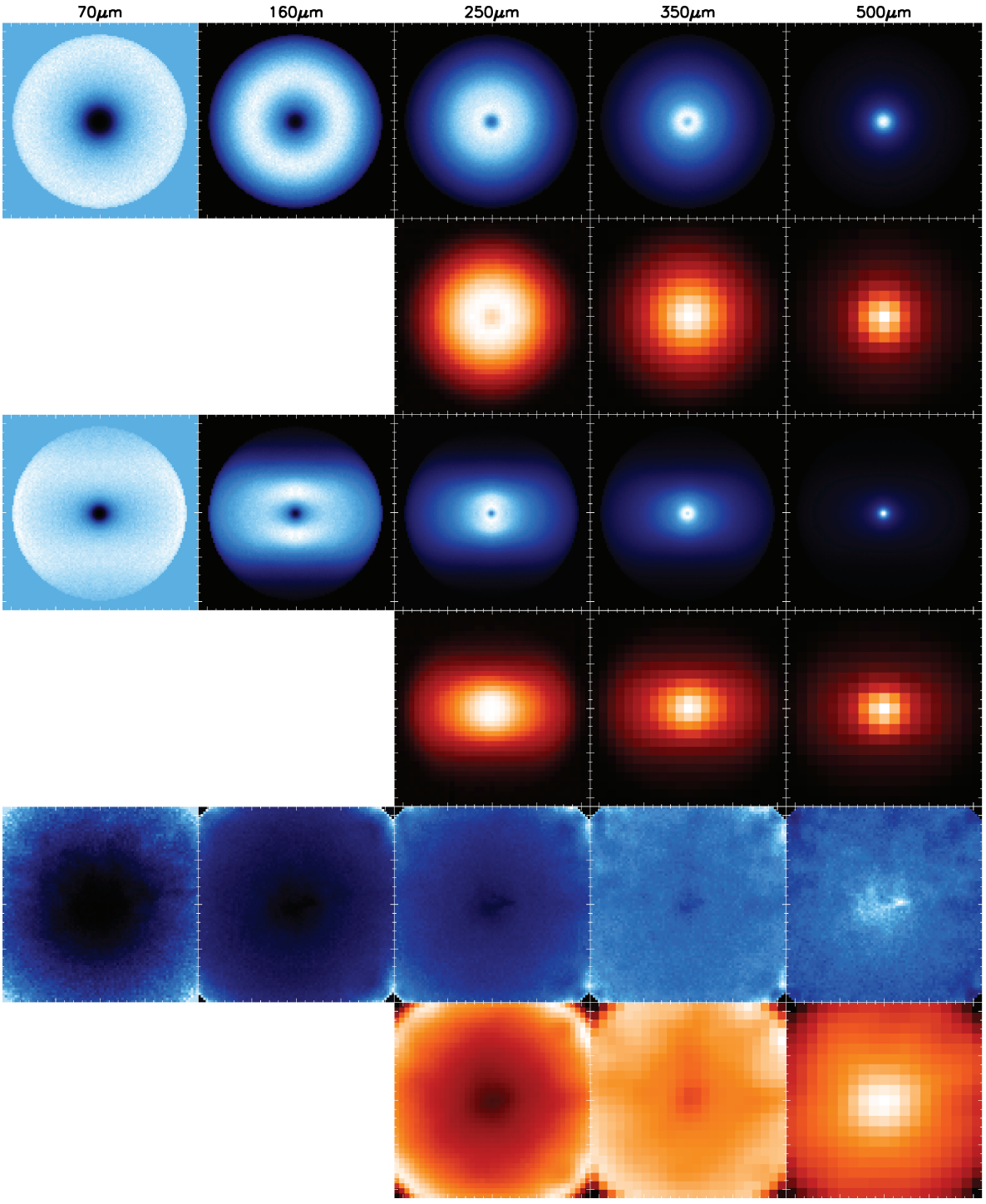

Figure 8. A grid of maps of the three model IRDCs shown by wavelength. The wavelength is listed at the top of each column. The first, third and fifth rows show the intensity maps from the radiative transfer modelling for the spherical, flattened and turbulent clouds, respectively. The second, fourth and sixth rows show the map from the row above (250–500 μm only) after it has been processed by the SPIRE telescope simulator. The radiative transfer models are shown with a blue colour table, the simulated observations are shown with a red colour table. The individual maps are linearly scaled between zero intensity (black) and maximum on the map (white).

each bin. For the model clouds we use a bin width equal to the pixel size. This is 2.9 arcsec (0.029 pc).

The top row of Fig. 9 shows the distribution of mean intensity versus equivalent semimajor axis for each of the eight model bands. The flux density has been normalized for clarity, but no minimum flux has been subtracted (i.e. zero on the relative scale equates to zero on the absolute scale). The colour key for each band is shown beneath Fig. 9. All three clouds show the characteristic IRDC extinction holes at PACS equivalent wavelengths (70 and 160 μm). The spherical and flattened clouds are completely extinguished at

Table 2. The geometry of the plane-of-the-sky intensity distribution towards each of the model clouds.

IRDC	Observed FWHM (pc)		
	(250 μm)	(350 μm)	(500 μm)
Spherical	0.563 × 0.565	0.474 × 0.474	0.262 × 0.263
Flattened	0.565 × 0.368	0.509 × 0.331	0.341 × 0.218
Turbulent	–	–	1.31 × 1.31

0.2–0.3 pc, but the turbulent cloud is extinguished across its entire radius (due to its higher mass).

The middle row of Fig. 9 shows the profiles of the three SPIRE bands. The model profile, from the upper row, is reproduced as a dashed line. Plotted over this is the profile of the simulated observation. The process of observing the clouds causes flux to be averaged out due to the resolution limit of the telescope. This moves flux towards regions of lower flux, i.e. outward or towards central holes, and is most pronounced for bands where there is a significant central dip in the model profiles.

The lower panel of Fig. 9 shows the results of fitting an optically thin $\beta = 1.85$ (Ossenkopf & Henning 1994) grey body to the radial SED of each cloud. The blue and purple curves show the best-fitting temperature for a grey body fitted to the 250–500 μm and 160–500 μm model cloud profiles, respectively (i.e. using the results of the radiative transfer model). The error bars show the grey body fitted to the 250–500 μm simulated observation profiles (i.e. taking into account instrumental effects). These are interpolated to the lowest common resolution (500 μm) before fitting the grey body.

These figures show that temperatures fitted to the observed fluxes match the temperatures that would have been fitted to the model IRDCs in the absence of instrumental effects. However, the fitted temperatures are higher than the actual temperatures (i.e. the ones calculated with the radiative transfer model) in the centre of the cloud and lower than the actual temperatures at the outer parts of the cloud. This is because the dust temperature from the simulated observations corresponds to an averaged temperature in the observed column, just as in real observations.

This demonstrates that for accurately determining the dust temperatures in IRDCs, detailed radiative transfer modelling is needed along with multiwavelength, spatially resolved observations. Accurate dust temperatures are important for determining the masses of these clouds. Previous studies have shown that overestimating cloud dust temperatures even by a few degrees may lead to underestimating cloud masses by a factor of 2–3 (Stamatellos et al. 2007). This has important implications for the inferred cloud stability and for the derived mass function of IRDCs.

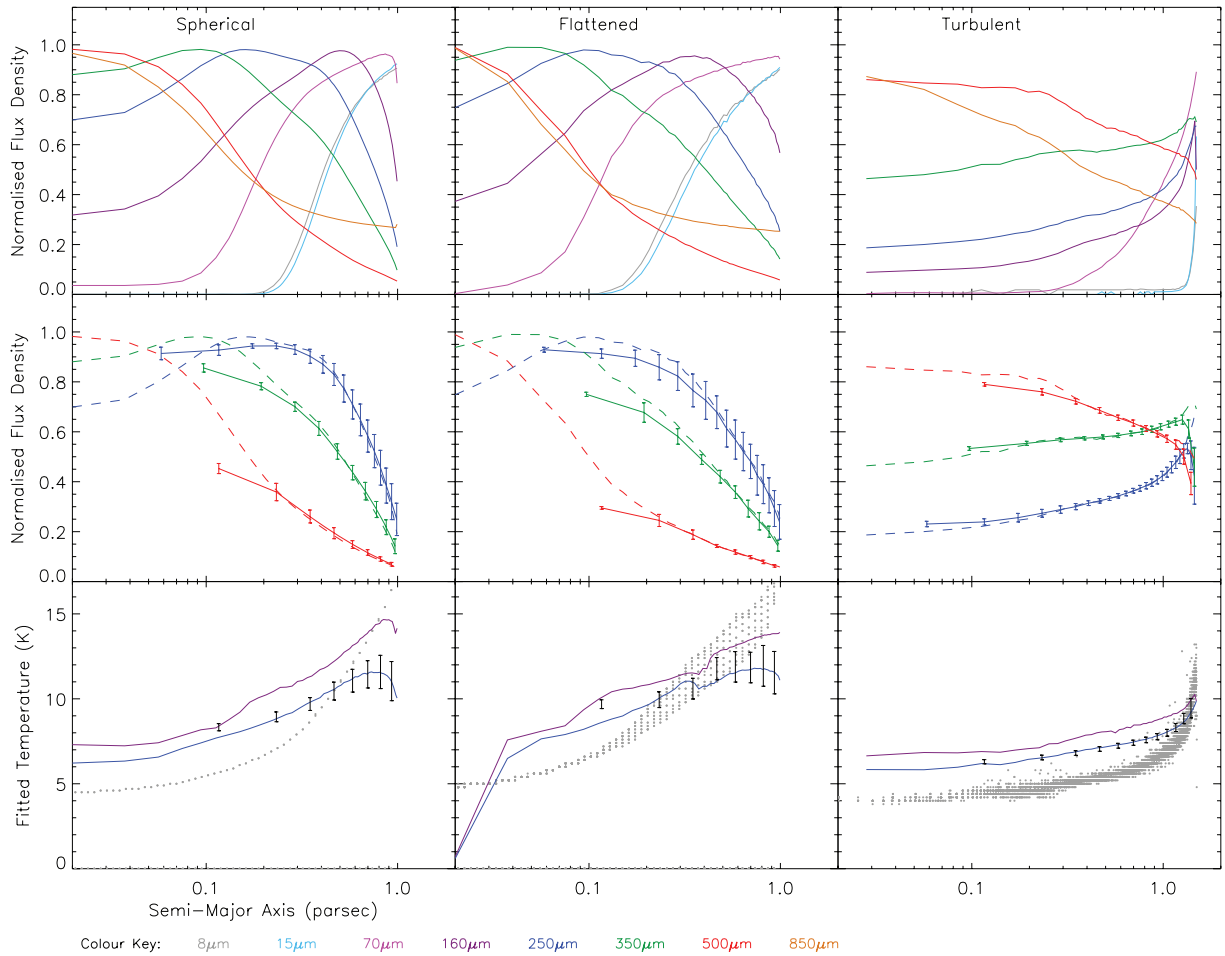

Figure 9. Radial profiles of the three model IRDCs at wavelengths 8–850 μm (top row). Flux from the simulated observations (solid lines and error bars) versus the radiative transfer model flux (dashed lines) at the SPIRE bands (middle row). SED fitted temperature using just the SPIRE bands (blue curve) and the SPIRE bands plus 160 μm (purple curve). The equivalent fit using the three SPIRE simulated maps is shown by the error bars. The dots correspond to the actual dust temperature computed by the radiative transfer models (bottom row).

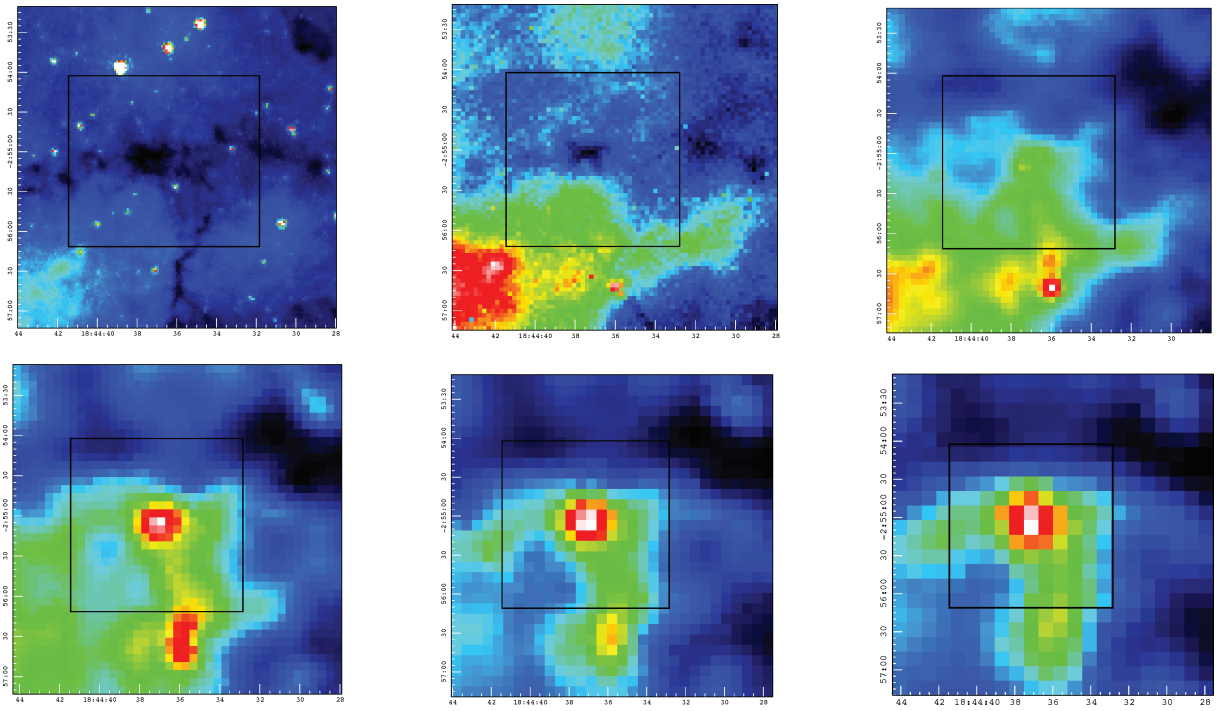

Figure 10. G29.55+00.18 observations at six wavebands (top row: 8-μm *Spitzer*/GLIMPSE, 70- and 170-μm PACS; bottom row: 250-, 350- and 500-μm SPIRE). The cloud is seen in absorption against the bright background at 8 and 70 μm, and in emission at longer wavelengths.

The methodology to determine the actual properties of an IRDC is to fit the observed fluxes at all available wavebands, by varying the assumed density structure of the radiative transfer model. The density structure can be spherically symmetric or axisymmetric (e.g. flattened core), depending on each specific cloud. 3D modelling is also possible, but the determined density structure cannot be uniquely recovered (e.g. Steinacker et al. 2003, 2005). Once the observed fluxes are fitted, the density profile of the cloud is determined, and the actual dust temperatures are calculated through the radiative transfer model.

6 G29.55+00.18, AN IRDC FROM THE HI-GAL SURVEY

G29.55+00.18 (Simon et al. 2006) is an IRDC, which has been observed by *Herschel*/PACS and *Herschel*/SPIRE as part of the Hi-GAL survey, and by *Spitzer*/GLIMPSE. The cloud is seen in absorption against the bright background at 8 and 70 μm, and in emission at longer wavelengths (Fig. 10). The SED of the cloud is shown in Fig. 12.

Guided by the image of the cloud at 500 μm, we model this cloud using a 2D density profile (equation 2) with a ratio of optical depths $\tau_{\theta=90^\circ}/\tau_{\theta=0^\circ} = 1.55$. The input parameters of the model and the derived physical properties of the cloud are listed in Table 3. The mass of the cloud is constrained by the longer wavelength data, which are approximately column density profiles, as the effect of the temperature gradient is relatively weak. The temperature of the cloud is mainly constrained by the shorter wavelength data. To match these short-wavelength data, the external radiation field is enhanced by a factor of $f_{\rm ISRF} = 2.5$, when compared with the ISRF at the solar neighbourhood, which is consistent with the higher ambient radiation field in the Galactic plane.

Table 3. The physical properties of the IRDC G29.55+00.18. $R_{\rm cloud}$: radius; r_0: flattening radius; $n_c(\rm H_2)$: central density; $\tau_{\theta=90^\circ}/\tau_{\theta=0^\circ}$: ratio of the visual optical depths; $f_{\rm ISRF}$: ISRF factor (see text); $T_{\rm SED}$: temperature calculated from a single-temperature, grey-body fitting of the SED; $T_{\rm model}$: temperature from the radiative transfer model; $M_{\rm SED}$: mass calculated from Hildebrand (1983) and $T_{\rm SED}$, $M_{\rm model}$: mass calculated from the radiative transfer model. The distance is taken from Heyer et al. (2009).

G29.55+00.18	
RA (2000)	18:44:37.00
Dec. (2000)	−02:55:07
Distance (kpc)	4.8
$R_{\rm cloud}$ (pc)	1.7
r_0 (pc)	0.2
$n_c(\rm H_2)$ ($\rm cm^{-3}$)	2.8×10^4
$\tau_{\theta=90^\circ}/\tau_{\theta=0^\circ}$	1.55
$f_{\rm ISRF}$	2.5
$T_{\rm SED}$ (K)	16
$T_{\rm model}$ (K)	10–21
$M_{\rm SED}$ ($\rm M_\odot$)	530
$M_{\rm model}$ ($\rm M_\odot$)	520

The model reproduces well the images of the cloud at different wavelengths (Fig. 11). At shorter wavelengths (8, 70 μm) the cloud is seen in absorption (note that the background is not modelled, hence there is no actual correspondence with the observed background), and in emission at longer wavelengths ($\gtrsim$170 μm).

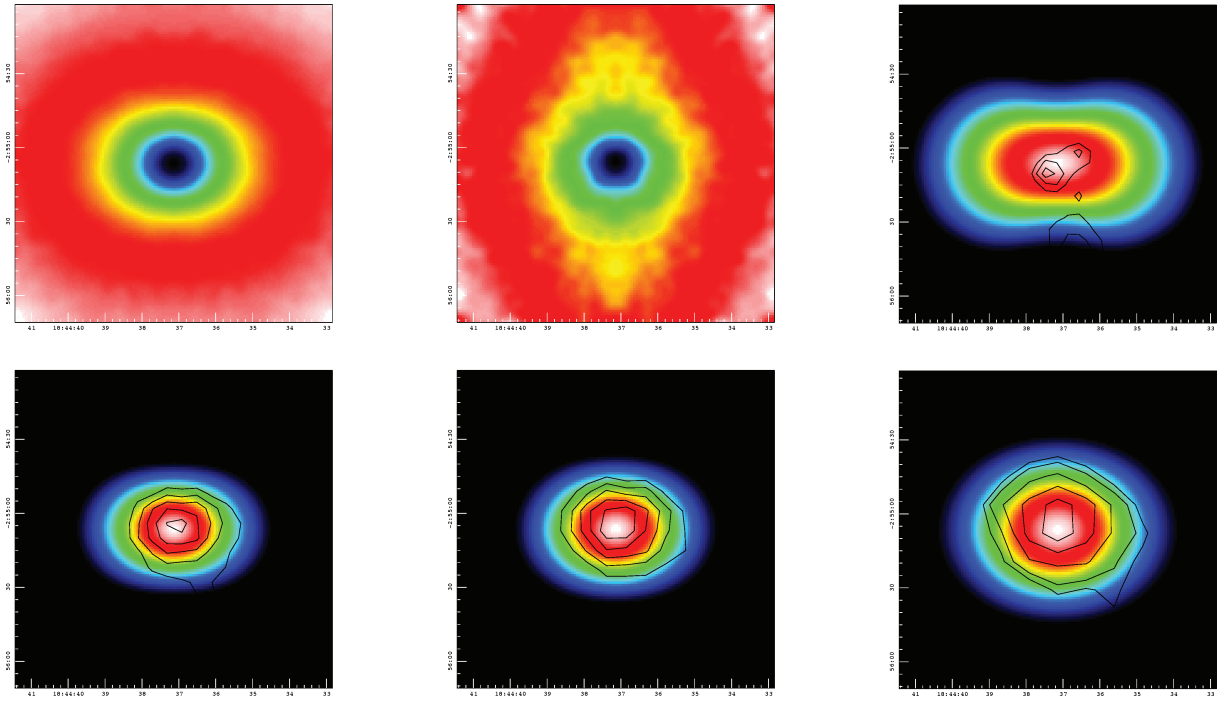

Figure 11. G29.55+00.18 simulated observations at six wavebands (same as in Fig. 10). Contours are taken from the observed data at the corresponding wavelength. The model reproduces the general characteristics of the appearance the core (flux and shape).

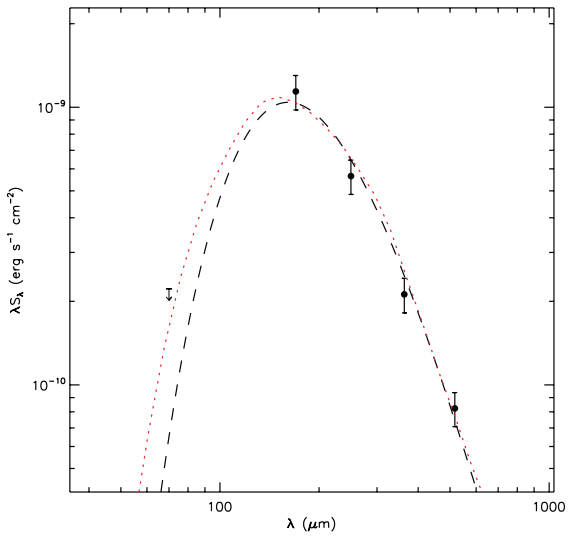

Figure 12. SED of G29.55+00.18. The dotted line corresponds to the SED calculated from the radiative transfer model, and the dashed line corresponds to the SED from a single-temperature, grey-body fit.

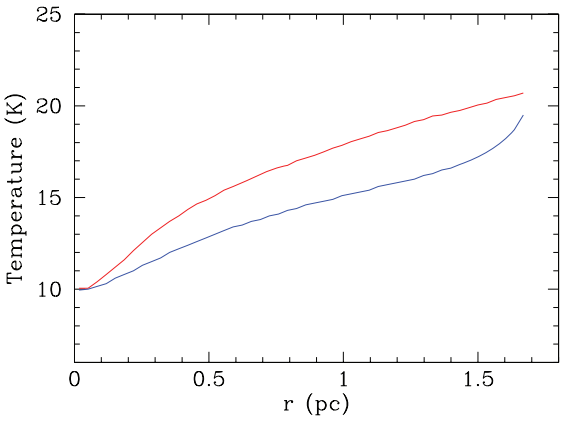

Figure 13. Dust temperature profile of G29.55+00.18 at two different directions in the cloud. The bottom line corresponds to the mid-plane of the flattened structure ($\theta = 90^\circ$), whereas the upper line corresponds to the direction perpendicular to the mid-plane ($\theta = 0^\circ$).

The flux and the shape of the cloud are well matched (assuming a viewing angle of $\theta_{\rm obs} = 40^\circ$). At 170 μm there is secondary peak that is not reproduced by the model. This is probably due to asymmetric heating as this secondary peak does not appear at longer wavelengths (cf. Nutter, Stamatellos & Ward-Thompson 2009); such heating is not included in the current model.

The observed SED is well fitted by the model (Fig. 12, dotted line). The dust temperature inside the cloud drops from 21 K at its edge to 10 K at its centre (Fig. 13; cf. Peretto et al. 2010). Additionally, there is a variance of the temperature with the polar angle θ, with the more dense region at the 'equator' of the cloud being colder by up to ∼3 K, as compared with the corresponding equal-radius region at the 'pole' of the cloud. The mass of the cloud is calculated to be 530 $M_\odot$.

We also compare the radiative transfer model with a simple grey-body single-temperature fitting of the SED. The SED is well reproduced using a temperature of 16 K (Fig. 12, dashed line). The mass of cloud calculated using the above temperature and the flux at 500 μm is 520 $M_\odot$, which is slightly lower but consistent with the mass obtained from the radiative transfer model, despite using an average, and not the actual, dust temperature. However, the inner dense regions of the cloud where star formation will occur are colder (by ∼5 K) than the estimated average temperature.

This example demonstrates the need for radiative transfer modelling for determining the temperature structure of IRDCs. Despite the fact that a simple grey-body single-temperature model provides a good fit to the SED, this model cannot accurately determine the temperature structure in the cloud and overestimates the temperature of the interesting, in terms of potential for star formation, inner dense regions of the cloud.

7 CONCLUSIONS

We have demonstrated the use of the 3D, multiwavelength Monte Carlo code PHAETHON to model the transfer of radiation in IRDCs, which are externally illuminated by the ISRF. The cores of these clouds are believed to be where high-mass stars form, i.e. they are the high-mass equivalent of pre-stellar clouds. We have presented three widely different models, in which we varied the mass, density, radius, morphology and internal velocity field of the cloud. We have shown the predicted output of the model at the wavebands of *Herschel* and *Spitzer*. We also passed the model output through the SPIRE simulator to produce simulated observations of these IRDCs. These were then analysed as if they were real observations. Subsequently, the results of this analysis were compared with the results of the radiative transfer modelling.

Our study highlights the need for detailed radiative transfer modelling when using multiwavelength observations from *Herschel* to accurately determine the properties of IRDCs. This method was applied for the study of G29.55+00.18, an IRDC from the Hi-GAL survey. Modelling of a larger sample of IRDCs found in the Hi-GAL survey will appear in a future publication (Wilcock et al., in preparation).

ACKNOWLEDGMENTS

We would like to thank the referee for his report that helped improving the original manuscript. Simulations were performed using the Cardiff HPC Cluster MERLIN. The colour plots of Fig. 5 were produced using SPLASH (Price 2007). DS and JMK acknowledge postdoctoral support from the Science & Technology Facilities Council (STFC) under the auspices of the Cardiff Astronomy Rolling Grant.

REFERENCES

André P., Bouwman J., Belloche A., Hennebelle P., 2003, in Curry C. L., Fich M., eds, Chemistry as a Diagnostic of Star Formation. NRC Press, Ottawa, Canada, p. 127
Baes M., Stamatellos D., Davies J. I., Whitworth A. P., Sabatini S., Roberts S., Linder S. M., Evans R., 2005, New Astron., 10, 523
Barnard E. E., Frost E. B., Calvert M. R., 1927, A Photographic Atlas of Selected Regions of the Milky Way. Carnegie Institution of Washington, Washington
Bjorkman J. E., Wood K., 2001, ApJ, 554, 615
Black J. H., 1994, in Cutri R. M., Latter W. B., eds, ASP Conf. Ser. Vol. 58, The First Symposium on the Infrared Cirrus and Diffuse Interstellar Clouds. Astron. Soc. Pac., San Francisco, p. 355
Carey S. J., Clark F. O., Egan M. P., Price S. D., Shipman R. F., Kuchar T. A., 1998, ApJ, 508, 721
Carey S. J., Feldman P. A., Redman R. O., Egan M. P., MacLeod J. M., Price S. D., 2000, ApJ, 543, L157
Egan M. P., Shipman R. F., Price S. D., Carey S. J., Clark F. O., Cohen M., 1998, ApJ, 494, L199
Fazio G. G. et al., 2004, ApJS, 154, 10
Flagey N., Boulanger F., Verstraete L., Miville Deschênes M., Noriega Crespo A., Reach W., 2006, A&A, 453, 969
Goodwin S. P., Whitworth A. P., Ward-Thompson D., 2004, A&A, 414, 633
Griffin M. et al., 2009, EAS Publ. Ser., 34, 33
Griffin M. J. et al., 2010, A&A, 518, L3
Heyer M., Krawczyk C., Duval J., Jackson J. M., 2009, ApJ, 699, 1092
Hildebrand R. H., 1983, QJRAS, 24, 267
Holland W. S. et al., 1999, MNRAS, 303, 659
Holland W. et al., 2006, Proc. SPIE, 6275, 45
Kawada M. et al., 2007, PASJ, 59, 389
Kirk J. M., Ward-Thompson D., André P., 2005, MNRAS, 360, 1506
Kirk J. M., Ward-Thompson D., Crutcher R. M., 2006, MNRAS, 369, 1445
Kirk J. M., Ward-Thompson D., André P., 2007, MNRAS, 375, 843
Li A., Draine B. T., 2001, ApJ, 554, 778
Lynds B. T., 1962, ApJS, 7, 1
Mathis J. S., Rumpl W., Nordsieck K. H., 1977, ApJ, 217, 425
Molinari S. et al., 2010a, PASP, 122, 314
Molinari S. et al., 2010b, A&A, 518, L100
Nutter D., Stamatellos D., Ward-Thompson D., 2009, MNRAS, 396, 1851
Ossenkopf V., Henning T., 1994, A&A, 291, 943
Parsons H., Thompson M. A., Chrysostomou A., 2009, MNRAS, 399, 1506
Pascale E. et al., 2008, ApJ, 681, 400
Perault M. et al., 1996, A&A, 315, L165
Peretto N., Fuller G. A., 2009, A&A, 505, 405
Peretto N. et al., 2010, A&A, 518, L98
Pilbratt G. L. et al., 2008, Proc. SPIE, 7010, 2
Pilbratt G. L. et al., 2010, A&A, 518, L1
Plummer H. C., 1915, MNRAS, 76, 107
Poglitsch A., Altieri B., 2009, EAS Publ. Ser., 34, 43
Poglitsch A. et al., 2010, A&A, 518, L2
Price D. J., 2007, Publ. Astron. Soc. Aust., 24, 159
Price S. D., Egan M. P., Carey S. J., Mizuno D. R., Kuchar T. A., 2001, AJ, 121, 2819
Rathborne J. M., Jackson J. M., Simon R., Zhang Q., 2009, Ap&SS, 324, 155
Rieke G. H. et al., 2004, Proc. SPIE, 5487, 50
Sibthorpe B., Chanial P., Griffin M. J., 2009, A&A, 503, 625
Simon R., Jackson J. M., Rathborne J. M., Chambers E. T., 2006, ApJ, 639, 227
Stamatellos D., 2003, PhD thesis, Cardiff University
Stamatellos D., Whitworth A. P., 2003, A&A, 407, 941
Stamatellos D., Whitworth A. P., 2005, A&A, 439, 153
Stamatellos D., Whitworth A. P., André P., Ward-Thompson D., 2004, A&A, 420, 1009
Stamatellos D., Whitworth A. P., Boyd D. F. A., Goodwin S. P., 2005, A&A, 439, 159
Stamatellos D., Whitworth A. P., Ward-Thompson D., 2007, MNRAS, 379, 1390
Steinacker J., Henning T., Bacmann A., Semenov D., 2003, A&A, 401, 405
Steinacker J., Bacmann A., Henning T., Klessen R., Stickel M., 2005, A&A, 434, 167
Ward-Thompson D., Scott P. F., Hills R. E., Andre P., 1994, MNRAS, 268, 276
Ward-Thompson D., André P., Crutcher R., Johnstone D., Onishi T., Wilson C., 2007, in Reipurth B., Jewitt D., Keil K., eds, Protostars and Planets V. Univ. Arizona Press, Tucson, p. 33
Whitworth A. P., Ward-Thompson D., 2001, ApJ, 547, 317
Zinnecker H., Yorke H. W., 2007, ARA&A, 45, 481

This paper has been typeset from a TEX/LATEX file prepared by the author.